

Earth system response to Heinrich events explained by a bipolar convection seesaw

Received: 30 January 2025

Accepted: 5 September 2025

Published online: 3 October 2025

 Check for updates

Matteo Willeit¹✉, Andrey Ganopolski¹, Christine Kaufhold^{1,2}, Daniela Dalmonch³, Bo Liu^{4,5} & Tatiana Ilyina^{4,5,6}

Abrupt climate changes repeatedly occurred during glacial periods, caused by intrinsic instabilities of the Atlantic Meridional Overturning Circulation (AMOC) leading to Dansgaard–Oeschger events, and by the AMOC's response to massive iceberg discharges in the North Atlantic, known as Heinrich events. This AMOC-driven millennial-scale climate variability is most prominent in the North Atlantic but also propagates to the Southern Ocean, where its imprint is particularly strong during cold (Stadial) phases featuring Heinrich events. Here we use an Earth system model to show that the qualitative differences between Heinrich Stadials and non-Heinrich Stadials seen in proxy records can be explained by a sudden start of convection in the Southern Ocean triggered by a strong weakening of the AMOC during Heinrich events. The sudden convection onset leads to rapid warming and sea ice retreat in the Southern Ocean, and the resulting ventilation of the deep ocean explains the rapid CO₂ increase of ~15 ppm on centennial timescales during some Heinrich Stadials. We propose a general mechanism whereby a shutdown of convection in the North Atlantic triggers convection in the Southern Ocean—a phenomenon we refer to as a bipolar convection seesaw—which could also be activated by a potential future weakening of the AMOC.

There is widespread evidence of pronounced Atlantic Meridional Overturning Circulation (AMOC) variability during glacial times associated with Dansgaard–Oeschger (DO) and Heinrich (H) events^{1–5}. It is now widely accepted that DO events⁶ can occur as part of internal variability of the ocean–sea ice–atmosphere system⁷ involving spontaneous transitions between weak and strong AMOC modes under certain boundary conditions^{8–10}, with alternating cold (Stadial) and warm (Interstadial, IS) conditions in the North Atlantic (NA). In addition, H events associated with large discharges of icebergs in the NA occurred repeatedly during glacial times^{11–13} and forced a weakening or collapse of the AMOC^{4,14} through the input of large amounts of freshwater into the NA¹⁵. Stadials containing H events are referred to as Heinrich Stadials (HSs).

While DO events have a large effect on the climate over Greenland¹⁶ and generally at high northern latitudes in the NA¹⁷, some H events also have a large impact on climate at high latitudes in the

Southern Hemisphere (SH)¹⁸. In particular, it has been noted that HSs and non-Heinrich Stadials (nHSs), which are almost indistinguishable in Greenland ice core records, have a very distinct imprint on Antarctic climate and atmospheric greenhouse gases. Several proxy records hint at qualitative differences between HSs and nHSs that cannot be explained solely by changes in AMOC strength: (1) a large and abrupt CO₂ increase by ~10–15 ppm on centennial timescales during HSs as opposed to a steady decrease of CO₂ during nHSs^{19–22}, (2) a large and abrupt warming of 2–3 °C over Antarctica during HSs^{18,23} and (3) a sudden jump in atmospheric methane concentration during HSs²⁴. Various proxies point to a crucial role played by the Southern Ocean (SO) to explain the peculiar dynamics during HSs, in particular through an increased ventilation of the SO^{25–30}, caused by shifts in the westerlies^{21,31–33}, enhanced convection and deep water formation^{28,29,34,35}, or a combination of the two processes³⁶.

¹Earth System Analysis, Potsdam Institute for Climate Impact Research, Member of the Leibniz Association, Potsdam, Germany. ²Institute of Physics and Astronomy, Universität Potsdam, Potsdam, Germany. ³Forest Modelling Laboratory, Institute for Agriculture and Forestry Systems in the Mediterranean, National Research Council of Italy (CNR-ISAFOM), Perugia, Italy. ⁴Universität Hamburg, Hamburg, Germany. ⁵Max Planck Institute for Meteorology, Hamburg, Germany. ⁶Helmholtz-Zentrum Hereon, Geesthacht, Germany. ✉e-mail: willeit@pik-potsdam.de

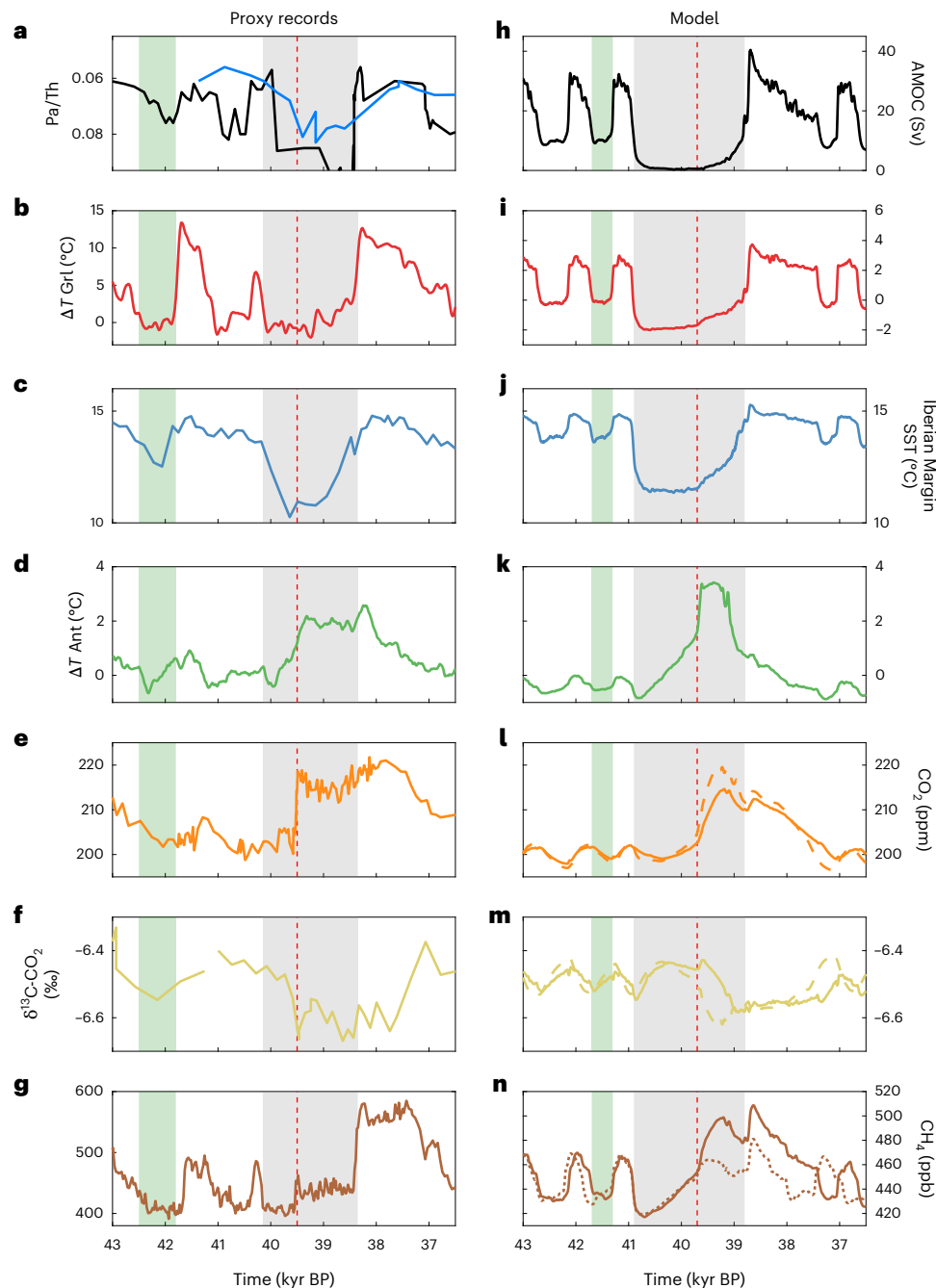


Fig. 1 | Proxy-model comparison of millennial climate variability.

a–n, Comparison of simulated (**h–n**) climate variability with proxy reconstructions (**a–g**) for a time interval around HS4: strength of the AMOC (ref. 4 in black and ref. 57 in blue) (**a** and **h**); Greenland (GrI) temperature¹⁶ (**b** and **i**); Iberian Margin sea surface temperature (SST)⁵⁸ (**c** and **j**); Antarctic (Ant) temperature averaged over four ice cores²³ (**d** and **k**); atmospheric CO₂ concentration^{20,21} (**e** and **l**); δ¹³C of CO₂ (ref. 49) (**f** and **m**); and CH₄ concentration²⁴

(**g** and **n**). The dashed lines in **l** and **m** show results of a model simulation where the land carbon cycle is not active. The dotted line in **n** shows the CH₄ concentration in a simulation with a prescribed constant CO₂ of 200 ppm. The shaded areas indicate the HS4 (grey) and a nHS (green). The vertical dashed red lines mark the timing of the jump in CH₄ and CO₂ in the left column and the onset of convection in the SO in the right column.

However, modelling studies so far have failed to realistically reproduce the timing and amplitude of Antarctic temperature and atmospheric CO₂ variations in response to freshwater hosing in the NA^{37–45}, except for simulations where convection in the SO was enforced to occur by applying an artificial negative freshwater flux at the surface in the SO³⁴. Therefore, a mechanistic understanding of the relation between Northern Hemisphere (NH) and SH climate response to AMOC variations during H events remains elusive. Here we use a fast Earth system model with fully interactive carbon cycle to investigate the Earth

system evolution during DO and H events and show that deep convection is triggered in the SO as a response to a strong AMOC weakening following some H events, explaining the observed large and abrupt Antarctic warming and atmospheric CO₂ increase.

Simulated millennial-scale climate variability

We use a fast Earth system model^{46,47} with interactive atmospheric CO₂ to simulate millennial-scale glacial climate variability (Methods). The model simulates spontaneous DO events under typical mid-glacial

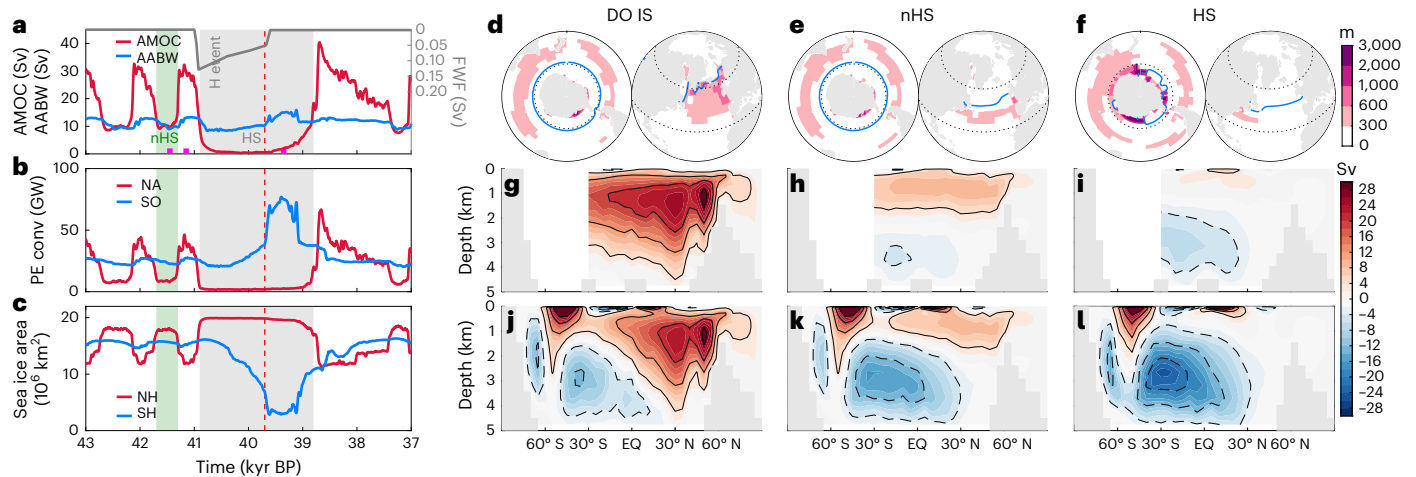


Fig. 2 | The bipolar convection seesaw. NA versus SO climate evolution in model simulations for mid-glacial conditions with internally generated DO events and a prescribed H event. **a**, Time series of the maximum of the AMOC streamfunction (red), Antarctic bottom water (AABW) formation rate (blue) and freshwater flux (FWF) applied to represent a H event in the NA (grey). **b**, Time series of the potential energy released by convection (PE conv) in the NA and the SO (south of 55° S). **c**, Time evolution of the maximum sea ice area in the two hemispheres.

The shaded areas in **a–c** indicate the HS and a nHS. The vertical dashed red lines mark the onset of convection in the SO. **d–f**, Maximum mixed layer depth for three time intervals marked by the magenta intervals in **a** representing DO IS (**d**), nHS (**e**) and HS (**f**) conditions. Blue lines indicate the maximum sea ice extent, and the dotted lines mark the parallels at 60° S and 30 and 60° N. EQ, equator. **g–l**, For the same three time periods, the Atlantic (**g–i**) and global (**j–l**) meridional overturning streamfunctions are also shown.

conditions¹⁰, with jumps between Stadials and ISs being associated with transitions between two different AMOC states¹⁰. We additionally mimic the effect of a H event iceberg discharge through a prescribed plausible input of a freshwater flux of -0.1 Sv (ref. 15) into the NA (Methods) and investigate the Earth system response to combined DO and H events in the model. The simulated H event is representative for the time interval around HS4 (Methods), which has been particularly extensively studied with many different high-resolution proxy records available for this period of time (Fig. 1).

The model captures the shape of the temperature response over Greenland (Fig. 1b,i), reflecting mainly DO variability associated with transitions in the AMOC state. At the Iberian Margin, the sea surface cooling during the HS is as much as three times larger than during nHSs (Fig. 1c,j). Over Antarctica, temperatures increase rapidly during the middle of the HS, by -3 – 4 °C in the model and by -2 – 3 °C in proxy data. By contrast, during nHSs, the temperature increase is about three to five times smaller and occurs more gradually over the entire duration of the Stadial (Fig. 1d,k).

The simulated CO₂ response to DO variability is generally within -5 ppm, in agreement with observations (Fig. 1e,l) and previous modelling results⁴⁴. However, during the HS, the model simulates a rapid increase in atmospheric CO₂ by -15 ppm (Fig. 1e,l), in good agreement with ice core records^{20,21}. In the model, the CO₂ response is partly dampened by the land carbon cycle absorbing part of the CO₂ released by the ocean (Fig. 1l), while a recent study suggests that substantial increases in biomass burning, which is not represented in our model, could have contributed to the very rapid initial increase and temporary overshoot seen in CO₂ ice core data during some HSs⁴⁸. The increase in CO₂ is accompanied by a simulated -0.2% decrease in $\delta^{13}\text{C}-\text{CO}_2$, consistent with ice core data⁴⁹ (Fig. 1f,m). The model also qualitatively reproduces the response of atmospheric CH₄ concentration to DO and H variability (Fig. 1g,n).

Overall, the model reproduces the main features of climate and carbon cycle variability associated with DO and H events, in particular the qualitative differences between HSs and nHSs.

SO convection during HSs

The simulated millennial-scale climate variability is tightly linked to AMOC variations (Fig. 2a). The Atlantic Ocean circulation is

fundamentally different during some HSs compared with nHSs, with proxy data supporting a strong AMOC response during HS4 (Fig. 1a,h). nHSs are characterized by a substantially weaker AMOC compared with ISs (Fig. 2g,h), but with convection still active at several locations in the NA (Fig. 2d,e), while the large freshwater input associated with the strong H event 4 leads to a rapid stop of convection and eventual shutdown of the AMOC in the model (Fig. 2f,i). Initially, this results in a widespread cooling in the NA region, but only limited localized warming in the South Atlantic. However, around 1,000 years after the AMOC collapse, deep convection first develops in the Ross Sea (Extended Data Fig. 1) and after some time rapidly spreads around Antarctica (Fig. 2b,f). The enhanced deep convection in the SO also leads to a strengthening of Antarctic bottom water formation (Fig. 2a,k,l). Although there are no direct proxies for SO circulation changes, there is ample evidence for an increased ventilation of the deep SO during past H events. Deep-water cooling²⁹ (Extended Data Fig. 2c), decreased radiocarbon ventilation ages²⁸ (Extended Data Fig. 2f), increased oxygenation of the deep SO²⁶ (Extended Data Fig. 2i) and an increase in primary productivity due to increased nutrient upwelling³¹ (Extended Data Fig. 3f) all provide support for a more vigorous convection in the SO. Convection in the SO then eventually stops after ~ 500 years, as soon as the AMOC starts to recover and convection resumes in the NA (Fig. 2a,b and Extended Data Fig. 1).

The abrupt onset of convection has a pronounced impact on climate at high southern latitudes (Fig. 3b), resulting in a large warming due to heat released from the deep ocean and consequent large retreat of sea ice (Figs. 2c and 3b). The increase in SO ventilation (Fig. 3f) resulting from the enhanced convection and the associated sea ice retreat brings large amounts of carbon that were stored in the deep ocean (Fig. 3h and Extended Data Fig. 2l) in contact with the atmosphere, leading to a rapid release of carbon (Fig. 3d) and a CO₂ increase of -15 ppm within a few centuries (Fig. 1l).

Rhodes et al. (2015)²⁴ suggested that the jump in CH₄ seen in ice core records during HS1 reflects the beginning of the H event, and this argument has been extended also to previous H events⁵⁰. However, our results show that the CH₄ jump in the middle of the HSs rather reflects the timing of the onset of convection in the SO, which is delayed by many centuries relative to the start of the actual H event. In our simulation, the CH₄ increase following convection

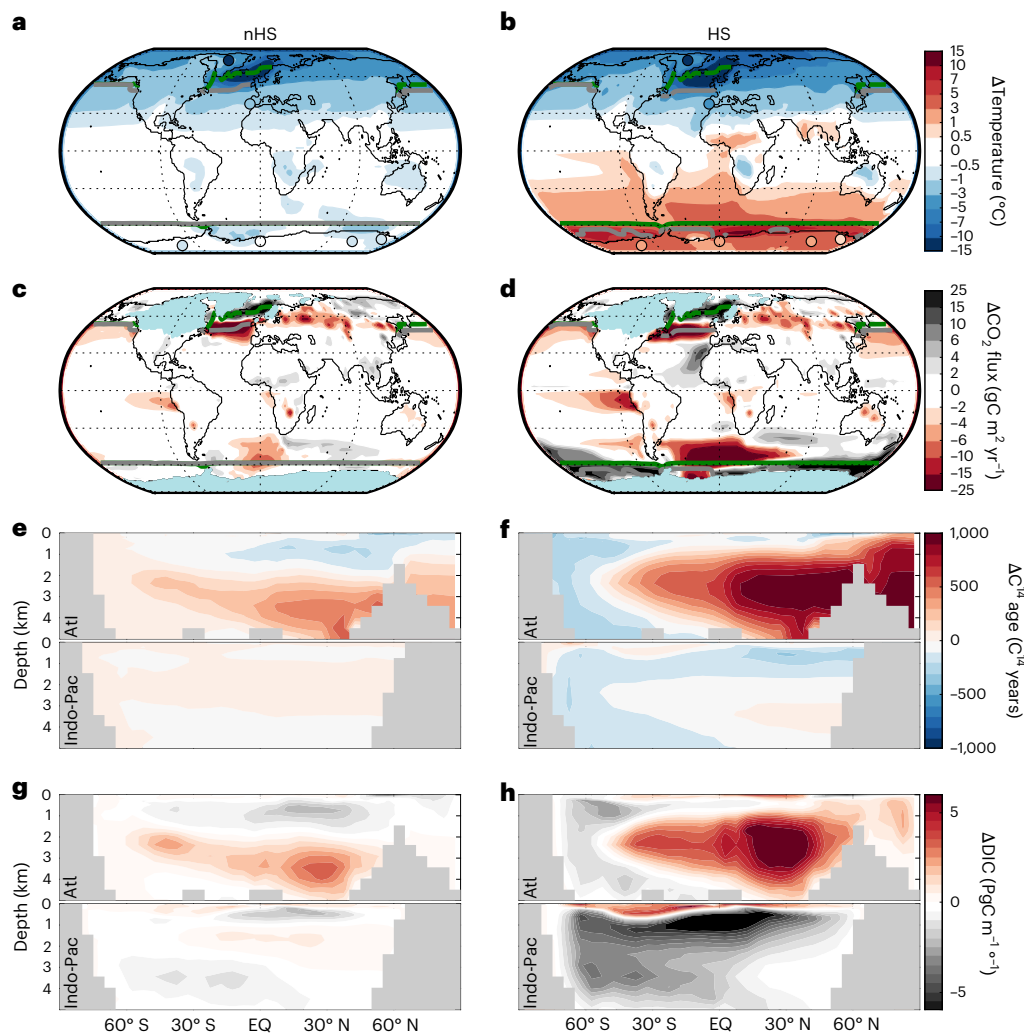


Fig. 3 | Climate and ocean biogeochemical changes during a DO cycle and an H event. **a–h**, Differences in simulated variables during nHSs (**a**, **c**, **e** and **g**) and HSs after the onset of SO convection (**b**, **d**, **f** and **h**) relative to IS conditions for annual mean near-surface air temperature (**a** and **b**), net carbon flux to the atmosphere (**c** and **d**), zonally averaged radiocarbon ventilation age (**e** and **f**) and zonally integrated dissolved inorganic carbon content (**g** and **h**). The filled circles

in **a** and **b** represent temperature changes estimated from proxy records^{16,23,58}. The green lines in **a–d** show the maximum sea ice extent during the IS, while the grey lines represent the maximum sea ice extent during nHS (**a** and **c**) and HS (**b** and **d**). All ocean fields in **e–h** are shown separately for the Atlantic Ocean (Atl) and the Indo-Pacific (Indo-Pac) Oceans, with the SO sectors being included.

onset in the SO is mainly a consequence of larger emissions from the tropics (Extended Data Fig. 3i), resulting from a combination of a general increase in precipitation over SH land (Extended Data Fig. 3c) and an increase in net primary production due to CO₂ fertilization (Extended Data Fig. 3f).

The bipolar convection seesaw

The term bipolar seesaw was originally introduced by Broecker (1998)⁵¹, who proposed an anti-phase response of deep sea ventilation in the NA and the SO to explain the Antarctic temperature response during the Younger Dryas. Later, Stocker and Johnsen (2003)⁵² introduced the thermal bipolar seesaw concept to explain the temperature response in Antarctica resulting from changes in the AMOC during glacial times. In their simple and purely thermodynamic model, the changes in meridional heat transport induced by AMOC changes combine with a heat reservoir in the SO to produce the Antarctic temperature response to AMOC perturbations. This simple model has since been widely invoked, with some refinements, to explain the relation between Greenland and Antarctic temperature evolution^{38,53,54}.

However, the thermal seesaw alone cannot explain the qualitative differences between nHSs and HSs. Skinner et al. (2020)²⁹ suggested

that convection in the SO occurred as a response to an AMOC weakening/collapse during HS4 in what they call a bipolar ventilation seesaw^{55,56}, which amplified Antarctic warming and the atmospheric CO₂ response. However, they do not relate the SO convection directly to the H event and can therefore not explain why convection would occur only during some HSs, but not during nHSs.

Here we propose that, to explain the observed millennial-scale glacial climate variability, the bipolar thermal seesaw should be complemented by the concept of a bipolar convective seesaw. The former always operates in response to AMOC changes via changes in interhemispheric heat transport. The latter operates only during some HSs, when the AMOC weakening is large enough to substantially affect salinity in the deep SO. An AMOC weakening generally leads to a salinity pile-up in the upper South Atlantic and a decrease in salinity in the deep Atlantic (Fig. 4b,c). In the case of an AMOC collapse following a H event, the response is generally more pronounced compared with the weak AMOC state during nHSs and the salinity decrease extends well into the deep SO (Fig. 4c). The resulting general salinity-induced destratification of the SO (Fig. 4h, Extended Data Figs. 4 and 5) creates the conditions for convection to start in the Ross Sea, an area that was already very close to convective instability

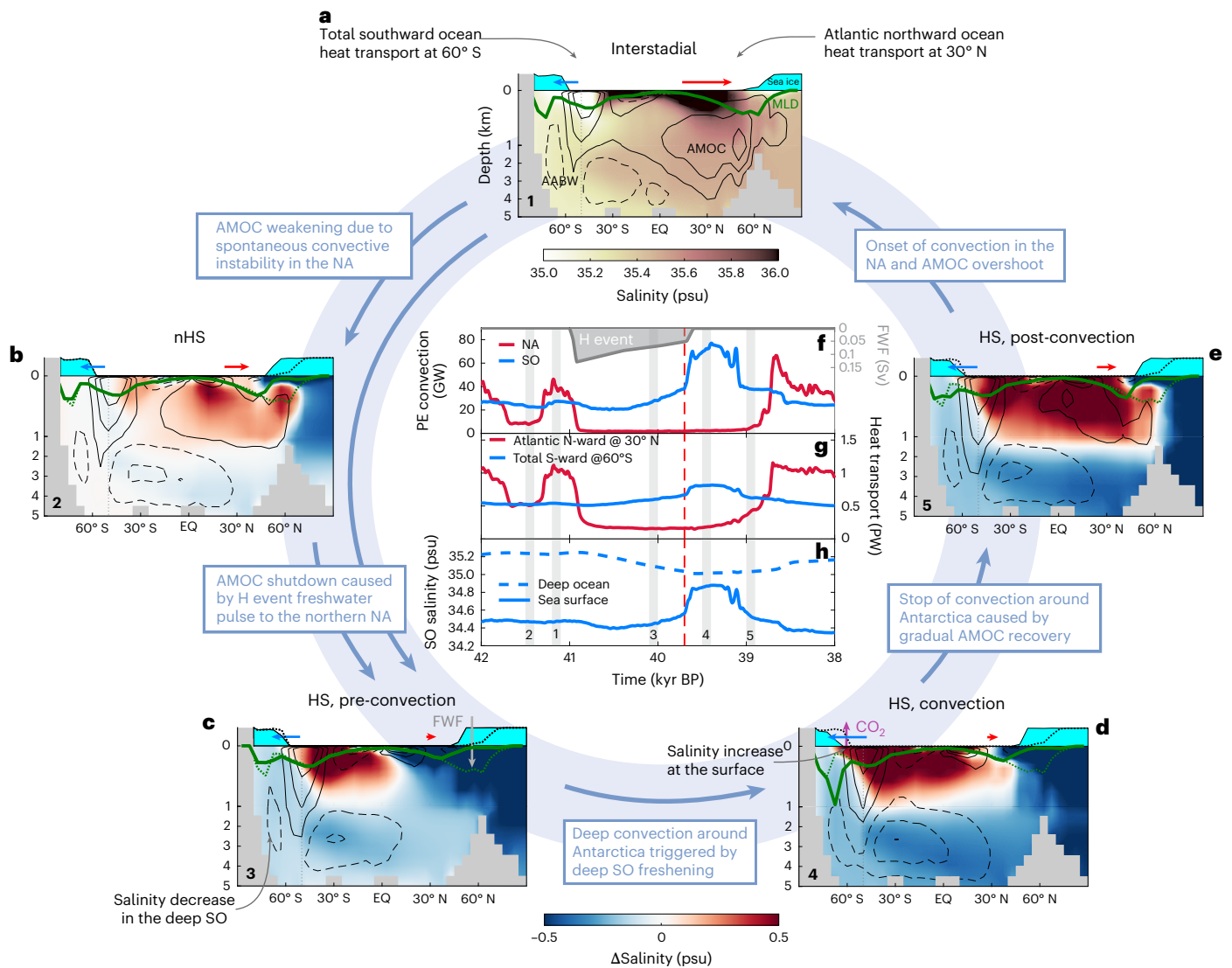


Fig. 4 | Bipolar convection seesaw mechanism. **a** IS state, showing Atlantic Ocean and SO (south of 50° S, dotted line) salinity, global overturning streamfunction (black; solid lines for clockwise and dashed lines for anti-clockwise circulation, drawn at steps of 8 Sv), zonally averaged sea ice concentration in the NA and SO, zonally averaged maximum mixed layer depth (MLD) (green line), northward Atlantic heat transport at 30° N (red arrow) and global southward heat transport at 60° S (blue arrow). **b**, The same as **a** but for nHSs, showing salinity differences relative to the IS. The dashed green line and

the dotted sea ice concentration show the reference IS state. **c–e**, The same as **b** but for the HS before (**c**), during (**d**) and after (**e**) convection in the SO. **f**, Potential energy (PE) released by convection, the same as Fig. 2b. **g**, Northward Atlantic heat transport at 30° N (red) and global southward heat transport at 60° S (blue). **h**, Average sea surface salinity and deep ocean salinity (below 1,000 m) in the SO (south of 60° S). The numbered time intervals marked in grey in **f–h** show the time slices represented in **a–e**.

(Extended Data Fig. 5a). Once convection starts somewhere, salty water from the deep ocean is mixed with low-salinity surface water, increasing sea surface salinity (Fig. 4d,h and Extended Data Fig. 4). This positive salinity anomaly then spreads horizontally, resulting in an increase in surface density in neighbouring areas, eventually cascading into large-scale convection. A positive feedback between deep convection and surface salinity enables the rapid expansion of convection around Antarctica. Temperature changes play only a secondary role for changes in stratification around Antarctica (Extended Data Figs. 4 and 5).

Convection in the SO is then sustained by an increased southward ocean heat transport in the SO (Fig. 4g), caused by the stronger SO overturning circulation associated with the enhanced Antarctic deep water formation (Fig. 2l). While the sea surface is efficiently cooled by the atmosphere, the subsurface warming resulting from the increased heat transport keeps convection going. As soon as the H event ends,

the AMOC slowly starts to recover (Fig. 2a), increasing also the northward ocean heat transport in the Atlantic and consequently decreasing the southward heat transport in the SH (Fig. 4g) until convection can no longer be sustained in the SO (Fig. 4e and Extended Data Fig. 1). The AMOC recovery is therefore the ultimate cause of the convection stop in the SO. This is further confirmed by additional simulations in which the Heinrich event is extended in duration, leading to a longer persistence of the AMOC off state (Extended Data Fig. 6c). Convection in the SO always remains active until the eventual recovery of the AMOC, keeping CO₂ levels and Antarctic temperature high throughout this time period (Extended Data Fig. 6f,i). The convective bipolar seesaw is thus fully controlled by AMOC dynamics. The quick resumption of the AMOC after the end of the H event occurs because the AMOC off state is not stable under the considered boundary conditions (Extended Data Fig. 7), leading to a spontaneous AMOC recovery once the freshwater forcing is removed.

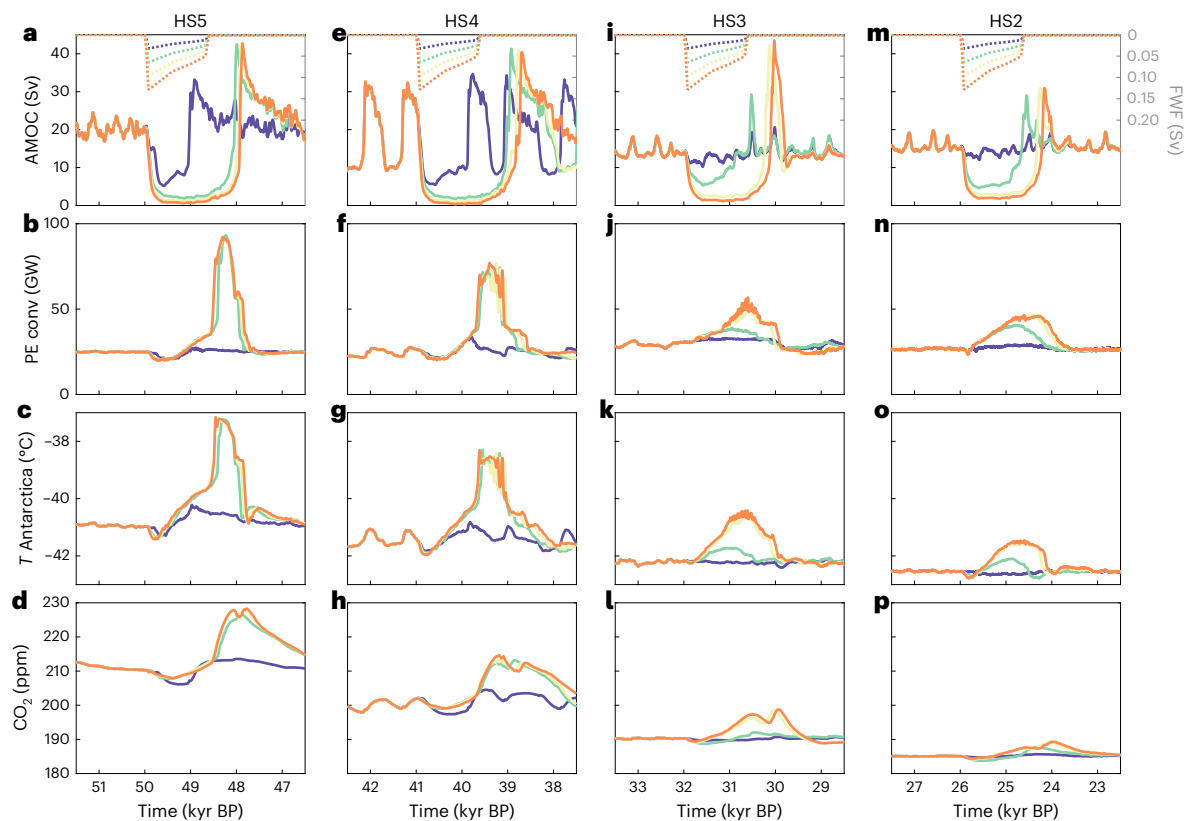


Fig. 5 | The bipolar seesaw during different HSs. a–p, Dependence of the simulated AMOC (**a, e, j and m**), potential energy released by convection (PE conv) in the SO (**b, f, j and n**), Antarctic temperature (**c, g, k and o**) and atmospheric CO₂ (**d, h, l and p**) to different boundary conditions (greenhouse gases concentration and orbital configuration) corresponding to the occurrence

of different HSs during the last glacial period (HS5, HS4, HS3 and HS2, from left to right), assuming a range of amplitudes of the H events (different colours). The dotted lines in the top panels (**a, e, i and m**) show the freshwater hosing flux (FWF) applied to the NA to mimic the different H events.

Robustness of the bipolar convection seesaw

The bipolar convection seesaw is a robust feature of our model. It does not depend on the timing of the H event during the DO cycles (Extended Data Fig. 6a,d,g) and is relatively insensitive to model parameters (Extended Data Fig. 8). It also works under very different boundary conditions in terms of CO₂ and ice sheets (Extended Data Fig. 9), although the amount of freshwater flux needed to weaken the AMOC sufficiently to trigger convection in the SO varies with changing boundary conditions. Changes in the SH westerlies are not needed to explain the Earth system response to H events in our model, as shown by a simulation with fixed wind stress (Extended Data Fig. 10).

H events occurred under different conditions in terms of orbital configuration and greenhouse gases concentrations, and reconstructions also indicate that the magnitude of ice discharge varied substantially across different H events¹⁵. The response seen in many proxies is large during some HSs, such as HS4 and HS5, but is less apparent during, for example, HS2 and HS3. Our results suggest that conditions during HS4 and HS5 were generally more favourable for a strong bipolar convection seesaw to operate (Fig. 5), with the response being additionally modulated by the magnitude of the H events and the amplitude of the induced AMOC weakening (Fig. 5 and Extended Data Fig. 6b,e,h). In our model, a very weak or collapsed AMOC is a necessary condition to produce a sufficient decrease in deep ocean salinity, which subsequently triggers convection in the SO, while it is clear that the weak AMOC state associated with nHSs (~10 Sv) does not have a sufficiently large impact on the stratification of the SO to trigger convection there.

The robustness of the proposed bipolar convection seesaw with respect to different climate and boundary conditions suggests that it could also operate in response to a possible future collapse of

the AMOC under global warming, with potentially large impacts on regional and global climate and the Antarctic ice sheet. We suggest that SO convection should be considered as a tipping element in the Earth system, with the bipolar convection seesaw forming a previously unidentified potential cross-hemispheric link between different tipping elements.

Online content

Any methods, additional references, Nature Portfolio reporting summaries, source data, extended data, supplementary information, acknowledgements, peer review information; details of author contributions and competing interests; and statements of data and code availability are available at <https://doi.org/10.1038/s41561-025-01814-0>.

References

1. Ganopolski, A. & Rahmstorf, S. Rapid changes of glacial climate simulated in a coupled climate model. *Nature* **409**, 153–8 (2001).
2. Rahmstorf, S. Ocean circulation and climate during the past 120,000 years. *Nature* **419**, 207–14 (2002).
3. Böhm, E. et al. Strong and deep Atlantic Meridional Overturning Circulation during the last glacial cycle. *Nature* **517**, 73–76 (2015).
4. Henry, L. G. et al. North Atlantic ocean circulation and abrupt climate change during the last glaciation. *Science* **353**, 470–474 (2016).
5. Lynch-Stieglitz, J. The Atlantic Meridional Overturning Circulation and abrupt climate change. *Annu. Rev. Mar. Sci.* **9**, 83–104 (2017).
6. Dansgaard, W. et al. Evidence for general instability of past climate from a 250-kyr ice-core record. *Nature* **364**, 218–220 (1993).

7. Menviel, L. C., Skinner, L. C., Tarasov, L. & Tzedakis, P. C. An ice-climate oscillatory framework for Dansgaard–Oeschger cycles. *Nat. Rev. Earth Environ.* **1**, 677–693 (2020).
8. Peltier, W. R. & Vettoretti, G. Dansgaard–Oeschger oscillations predicted in a comprehensive model of glacial climate: a “kicked” salt oscillator in the Atlantic. *Geophys. Res. Lett.* **41**, 7306–7313 (2014).
9. Malmierca-Vallet, I. & Sime, L. C. Dansgaard–Oeschger events in climate models: review and baseline Marine Isotope Stage 3 (MIS3) protocol. *Clim. Past* **19**, 915–942 (2023).
10. Willeit, M., Ganopolski, A., Edwards, N. R. & Rahmstorf, S. Surface buoyancy control of millennial-scale variations in the Atlantic meridional ocean circulation. *Clim. Past* **20**, 2719–2739 (2024).
11. Heinrich, H. Origin and consequences of cyclic ice rafting in the Northeast Atlantic Ocean during the past 130,000 years. *Quat. Res.* **29**, 142–152 (1988).
12. Bond, G. et al. Evidence for massive discharges of icebergs into the North Atlantic ocean during the last glacial period. *Nature* **360**, 245–249 (1992).
13. Hemming, S. R. Heinrich events: massive late Pleistocene detritus layers of the North Atlantic and their global climate imprint. *Rev. Geophys.* **42**, RG1005 (2004).
14. McManus, J. F., Francois, R., Gherardi, J.-M., Keigwin, L. D. & Brown-Leger, S. Collapse and rapid resumption of Atlantic meridional circulation linked to deglacial climate changes. *Nature* **428**, 834–7 (2004).
15. Zhou, Y. & McManus, J. F. Heinrich event ice discharge and the fate of the Atlantic Meridional Overturning Circulation. *Science* **384**, 983–986 (2024).
16. Kindler, P. et al. Temperature reconstruction from 10 to 120 kyr b2k from the NGRIP ice core. *Clim. Past* **10**, 887–902 (2014).
17. Sadatzki, H. et al. Sea ice variability in the southern norwegian sea during glacial dansgaard-oeschger climate cycles. *Sci. Adv.* **5**, 1–11 (2019).
18. Jouzel, J. et al. Orbital and millennial Antarctic climate variability over the past 800,000 years. *Science* **317**, 793–796 (2007).
19. Marcott, S. et al. Centennial-scale changes in the global carbon cycle during the last deglaciation. *Nature* **514**, 616–619 (2014).
20. Bauska, T. K., Marcott, S. A. & Brook, E. J. Abrupt changes in the global carbon cycle during the last glacial period. *Nat. Geosci.* **14**, 91–96 (2021).
21. Wendt, K. A. et al. Southern Ocean drives multidecadal atmospheric CO₂ rise during Heinrich Stadials. *Proc. Natl Acad. Sci. USA* **121**, 2017 (2024).
22. Nehrbass-Ahles, C. et al. Abrupt CO₂ release to the atmosphere under glacia and early interglacial climate conditions. *Science* **369**, 1000–1005 (2020).
23. Markle, B. R. & Steig, E. J. Improving temperature reconstructions from ice-core water-isotope records. *Clim. Past* **18**, 1321–1368 (2022).
24. Rhodes, R. H. et al. Enhanced tropical methane production in response to iceberg discharge in the North Atlantic. *Science* **348**, 1016–1019 (2015).
25. Gottschalk, J. et al. Biological and physical controls in the Southern Ocean on past millennial-scale atmospheric CO₂ changes. *Nat. Commun.* **7**, 11539 (2016).
26. Jaccard, S. L., Galbraith, E. D., Martínez-García, A. & Anderson, R. F. Covariation of deep Southern Ocean oxygenation and atmospheric CO₂ through the last ice age. *Nature* **530**, 207–210 (2016).
27. Rae, J. W. et al. CO₂ storage and release in the deep Southern Ocean on millennial to centennial timescales. *Nature* **562**, 569–573 (2018).
28. Li, T. et al. Rapid shifts in circulation and biogeochemistry of the Southern Ocean during deglacial carbon cycle events. *Sci. Adv.* **6**, 1–10 (2020).
29. Skinner, L., Menviel, L., Broadfield, L., Gottschalk, J. & Greaves, M. Southern Ocean convection amplified past Antarctic warming and atmospheric CO₂ rise during Heinrich Stadial 4. *Commun. Earth Environ.* **1**, 1–8 (2020).
30. Yu, J. et al. Millennial atmospheric CO₂ changes linked to ocean ventilation modes over past 150,000 years. *Nat. Geosci.* **16**, 1166–1173 (2023).
31. Anderson, R. F. et al. Wind-driven upwelling in the Southern Ocean and the deglacial rise in atmospheric CO₂. *Science* **323**, 1443–1448 (2009).
32. Buizert, C. et al. Abrupt ice-age shifts in southern westerly winds and Antarctic climate forced from the north. *Nature* **563**, 681–685 (2018).
33. Legrain, E. et al. Centennial-scale variations in the carbon cycle enhanced by high obliquity. *Nat. Geosci.* **17**, 1154–1161 (2024).
34. Menviel, L., Spence, P. & England, M. H. Contribution of enhanced Antarctic Bottom Water formation to Antarctic warm events and millennial-scale atmospheric CO₂ increase. *Earth Planet. Sci. Lett.* **413**, 37–50 (2015).
35. Pedro, J. B. et al. Southern Ocean deep convection as a driver of Antarctic warming events. *Geophys. Res. Lett.* **43**, 2192–2199 (2016).
36. Menviel, L. et al. Southern Hemisphere westerlies as a driver of the early deglacial atmospheric CO₂ rise. *Nat. Commun.* **9**, 1–12 (2018).
37. Kageyama, M. et al. Climatic impacts of fresh water hosing under last glacial maximum conditions: a multi-model study. *Clim. Past* **9**, 935–953 (2013).
38. Pedro, J. B. et al. Beyond the bipolar seesaw: toward a process understanding of interhemispheric coupling. *Quat. Sci. Rev.* **192**, 27–46 (2018).
39. Schmittner, A. & Galbraith, E. D. Glacial greenhouse-gas fluctuations controlled by ocean circulation changes. *Nature* **456**, 373–376 (2008).
40. Bouttes, N., Roche, D. M. & Paillard, D. Systematic study of the impact of fresh water fluxes on the glacial carbon cycle. *Clim. Past* **8**, 589–607 (2012).
41. Brovkin, V., Ganopolski, A., Archer, D. & Munhoven, G. Glacial CO₂ cycle as a succession of key physical and biogeochemical processes. *Clim. Past* **8**, 251–264 (2012).
42. Gottschalk, J. et al. Mechanisms of millennial-scale atmospheric CO₂ change in numerical model simulations. *Quat. Sci. Rev.* **220**, 30–74 (2019).
43. Nielsen, S. B., Jochum, M., Pedro, J. B., Eden, C. & Nuterman, R. Two-timescale carbon cycle response to an AMOC collapse. *Paleoceanogr. Paleoclimatol.* **34**, 511–523 (2019).
44. Jochum, M. et al. Carbon fluxes during Dansgaard–Oeschger events as simulated by an Earth system model. *J. Clim.* **35**, 5745–5758 (2022).
45. Saini, H., Meissner, K. J., Menviel, L. & Kvale, K. Transient response of Southern Ocean ecosystems during Heinrich Stadials. *Paleoceanogr. Paleoclimatol.* **39**, e2023PA004754 (2024).
46. Willeit, M., Ganopolski, A., Robinson, A. & Edwards, N. R. The Earth system model CLIMBER-X v1.0—part 1: climate model description and validation. *Geosci. Model Dev.* **15**, 5905–5948 (2022).
47. Willeit, M. et al. The Earth system model CLIMBER-X v1.0—part 2: the global carbon cycle. *Geosci. Model Dev.* **16**, 3501–3534 (2023).
48. Riddell-Young, B. et al. Abrupt changes in biomass burning during the last glacial period. *Nature* **637**, 91–96 (2025).

49. Bauska, T. K. et al. Controls on millennial-scale atmospheric CO₂ variability during the last glacial period. *Geophys. Res. Lett.* **45**, 7731–7740 (2018).
50. Martin, K. C. et al. Bipolar impact and phasing of Heinrich-type climate variability. *Nature* **617**, 100–104 (2023).
51. Broecker, W. S. Paleocean circulation during the last deglaciation: a bipolar seesaw? *Paleoceanography* **13**, 119–121 (1998).
52. Stocker, T. F. & Johnsen, S. J. A minimum thermodynamic model for the bipolar seesaw. *Paleoceanography* **18**, PA1087 (2003).
53. Barker, S. et al. 800,000 years of abrupt climate variability. *Science* **334**, 347–351 (2011).
54. Davtian, N. & Bard, E. A new view on abrupt climate changes and the bipolar seesaw based on paleotemperatures from Iberian Margin sediments. *Proc. Natl Acad. Sci. USA* **120**, 2017 (2023).
55. Skinner, L. C., Waelbroeck, C., Scrivner, A. E. & Fallon, S. J. Radiocarbon evidence for alternating northern and southern sources of ventilation of the deep Atlantic carbon pool during the last deglaciation. *Proc. Natl Acad. Sci. USA* **111**, 5480–5484 (2014).
56. Skinner, L. et al. Rejuvenating the ocean: mean ocean radiocarbon, CO₂ release, and radiocarbon budget closure across the last deglaciation. *Clim. Past* **19**, 2177–2202 (2023).
57. Burckel, P. et al. Changes in the geometry and strength of the Atlantic Meridional Overturning Circulation during the last glacial (20–50 ka). *Clim. Past* **12**, 2061–2075 (2016).
58. Martrat, B. et al. Four climate cycles of recurring deep and surface water destabilizations on the Iberian Margin. *Science* **317**, 502–507 (2007).

Publisher's note Springer Nature remains neutral with regard to jurisdictional claims in published maps and institutional affiliations.

Open Access This article is licensed under a Creative Commons Attribution 4.0 International License, which permits use, sharing, adaptation, distribution and reproduction in any medium or format, as long as you give appropriate credit to the original author(s) and the source, provide a link to the Creative Commons licence, and indicate if changes were made. The images or other third party material in this article are included in the article's Creative Commons licence, unless indicated otherwise in a credit line to the material. If material is not included in the article's Creative Commons licence and your intended use is not permitted by statutory regulation or exceeds the permitted use, you will need to obtain permission directly from the copyright holder. To view a copy of this licence, visit <http://creativecommons.org/licenses/by/4.0/>.

© The Author(s) 2025

Methods

Earth system model

We use the CLIMBER-X Earth system model^{46,47}, including the frictional-geostrophic three-dimensional ocean model GOLDSTEIN^{59,60} with 23 vertical layers, the semi-empirical statistical-dynamical atmosphere model SESAM⁴⁶, the dynamic-thermodynamic sea ice model SISIM⁴⁶, the land surface model with interactive vegetation PALADYN⁶¹ and the ocean biogeochemistry model HAMOCC6^{62–64}. The comprehensive carbon cycle in the model allows one to interactively compute the atmospheric CO₂ evolution. Here we use the ‘closed’ carbon cycle set-up, in which marine sediments and chemical weathering on land are ignored. In this set-up, carbon is conserved in the atmosphere–ocean–land system, which is a reasonable assumption on millennial scales. All components of the model have a horizontal resolution of 5° × 5°. Ice sheets are prescribed and the net freshwater flux from ice sheets is zero. The model is described in detail in ref. 46 and ref. 47 and in general shows performances that are comparable with state-of-the-art CMIP6 models under different forcings and boundary conditions. Notably, the model has been shown to reproduce DO-like variability under mid-glacial conditions¹⁰, and the stability of the AMOC in the model has been thoroughly explored⁶⁵.

Experiments

The main model experiment is designed to simulate realistic millennial-scale climate variability during glacial times, that is, Marine Isotope Stage 3, and more specifically a time interval around HS4. The boundary conditions for this simulation include mid-glacial ice sheets from the GLAC-ID reconstruction⁶⁶, a CH₄ concentration of 425 ppb, a N₂O concentration of 230 ppb and the orbital configuration of 40 kyr before present (BP). Similarly to ref. 10, we apply noise in the surface freshwater flux in the northern NA so that the model produces robust internal DO cycles. We first perform a model spin-up of 10,000 years with a prescribed atmospheric CO₂ concentration of 200 ppm, which is representative for the HS4 interval, to allow the climate and carbon cycle to reach an (oscillating) equilibrium state. Starting from that, we then run a 10,000-year-long simulation with interactive CO₂. In this simulation, we introduce a plausible H event starting in simulation year 2,200, during a DO IS phase. The prescribed temporal shape of the freshwater flux associated with the H iceberg discharge event is derived qualitatively using results of different ice sheet model simulations^{67–70}, with a peak freshwater flux of 0.13 Sv, followed by a gradual decline until the event ends around 1,200 years later (Fig. 2a). Spatially, the freshwater flux is added uniformly to the ice-rafted-debris belt in the NA, between 40° N and 60° N and between 10° W and 70° W. No compensation of the freshwater flux is applied, and the average ocean salinity decreases by -0.1 psu by the end of the H event.

To separate the effect of changes in wind stress over the ocean on the model response to DO and H events, we have run an additional simulation in which the seasonal wind stress fields are kept constant at their initial (nHS) state.

A simulation where only the ocean carbon cycle is allowed to contribute to the atmospheric CO₂ evolution, while the land carbon fluxes are ignored, was additionally performed to isolate the contribution of ocean carbon cycle processes to atmospheric CO₂.

To quantify the effect of CO₂ fertilization on the increase in CH₄ emissions following the onset of SO convection, we performed an additional simulation with the same boundary conditions as the reference model run, but in which atmospheric CO₂ is prescribed at a constant value of 200 ppm.

In addition to the reference model simulation, we performed a number of simulations to explore the sensitivity of the results to the amplitude (×0.25, ×0.5, ×0.75 and ×1.5), timing (H event starting at the beginning and in the middle of a Stadial) and duration of the H event (idealized constant 0.1 Sv freshwater flux for 1,000, 2,000, 3,000 and 4,000 years).

We also run an ensemble of simulations with perturbed parameters to assess the robustness of the results with respect to changes in ocean model parameters (minimum and maximum diapycnal diffusivities, Gent–McWilliams diffusivity and the maximum slope of the isopycnals). To avoid having to run a spin-up of the carbon cycle for each of the ensemble members, these experiments are run with a prescribed constant CO₂ of 200 ppm, starting from the same initial condition as the reference run, and the H event is applied starting from the year 3,000.

To explore the dependence of the results on the background climate conditions, the set of simulations for HS4 boundary conditions with different amplitudes of the H event were extended also to other time intervals during MIS3 corresponding to the times when HS5, HS3 and HS2 occurred. For HS5, we used CO₂ = 210 ppm, CH₄ = 450 ppb, N₂O = 240 ppb and an orbital configuration of 49 kyr BP. For HS3, we used CO₂ = 190 ppm, CH₄ = 400 ppb, N₂O = 215 ppb and an orbital configuration of 31 kyr BP. For HS2, we used CO₂ = 185 ppm, CH₄ = 375 ppb, N₂O = 200 ppb and an orbital configuration of 25 kyr BP. The orbital parameters are from ref. 71.

To further investigate the robustness of our results to a wider range of boundary conditions, we performed additional simulations with present-day and last glacial maximum ice sheets and with different constant CO₂ concentrations (180, 220 and 280 ppm). For this more idealized set of simulations, we used present-day orbital parameters. These simulations are run for 10,000 years, and the H event is applied starting in the year 5,000, to give the system enough time to equilibrate with the different boundary conditions. The initial condition for these experiments is a preindustrial equilibrium state. We also repeated these simulations with the amplitude of the H event halved and doubled.

Data availability

The output of the model simulations described in the Article are available via Zenodo at <https://doi.org/10.5281/zenodo.15696715> (ref. 72).

Code availability

The CLIMBER-X model code is available via GitHub at <https://github.com/cxesmc/climber-x>. For this study, we used the tagged v.1.4.0 of the model.

References

- Edwards, N. R., Willmott, A. J. & Killworth, P. D. On the role of topography and wind stress on the stability of the thermohaline circulation. *J. Phys. Oceanogr.* **28**, 756–778 (1998).
- Edwards, N. R. & Marsh, R. Uncertainties due to transport-parameter sensitivity in an efficient 3-D ocean-climate model. *Clim. Dyn.* **24**, 415–433 (2005).
- Willeit, M. & Ganopolski, A. PALADYN v1.0, a comprehensive land surface–vegetation–carbon cycle model of intermediate complexity. *Geosci. Model Dev.* **9**, 3817–3857 (2016).
- Ilyina, T. et al. Global ocean biogeochemistry model HAMOCC: model architecture and performance as component of the MPI-Earth system model in different CMIP5 experimental realizations. *J. Adv. Model. Earth Syst.* **5**, 287–315 (2013).
- Mauritsen, T. et al. Developments in the MPI-M Earth System Model version 1.2 (MPI-ESM1.2) and its response to increasing CO₂. *J. Adv. Model. Earth Syst.* **11**, 998–1038 (2019).
- Liu, B., Six, K. D. & Ilyina, T. Incorporating the stable carbon isotope ¹³C in the ocean biogeochemical component of the Max Planck Institute Earth System Model. *Biogeosciences* **18**, 4389–4429 (2021).
- Willeit, M. & Ganopolski, A. Generalized stability landscape of the Atlantic Meridional Overturning Circulation. *Earth Syst. Dyn.* **15**, 1417–1434 (2024).

66. Tarasov, L., Dyke, A. S., Neal, R. M. & Peltier, W. R. A data-calibrated distribution of deglacial chronologies for the North American ice complex from glaciological modeling. *Earth Planet. Sci. Lett.* **315–316**, 30–40 (2012).
67. Calov, R., Ganopolski, A., Petoukhov, V., Claussen, M. & Greve, R. Large-scale instabilities of the Laurentide ice sheet simulated in a fully coupled climate-system model. *Geophys. Res. Lett.* **29**, 1–4 (2002).
68. Ziemeň, F. A., Kapsch, M.-L., Klockmann, M. & Mikolajewicz, U. Heinrich events show two-stage climate response in transient glacial simulations. *Clim. Past* **15**, 153–168 (2019).
69. Alvarez-Solas, J., Robinson, A., Montoya, M. & Ritz, C. Iceberg discharges of the last glacial period driven by oceanic circulation changes. *Proc. Natl Acad. Sci. USA* **110**, 16350–4 (2013).
70. Schannwell, C., Mikolajewicz, U., Ziemeň, F. & Kapsch, M.-L. Sensitivity of Heinrich-type ice-sheet surge characteristics to boundary forcing perturbations. *Clim. Past* **19**, 179–198 (2023).
71. Laskar, J. et al. A long-term numerical solution for the insolation quantities of the Earth. *Astron. Astrophys.* **428**, 261–285 (2004).
72. Willeit, M. et al. Publication data for: ‘Earth system response to heinrich events explained by a bipolar convection seesaw’. *Zenodo* <https://doi.org/10.5281/zenodo.15696715> (2025).

Acknowledgements

M.W. is funded by the German climate modelling project PalMod supported by the German Federal Ministry of Education and Research (BMBF) as a Research for Sustainability initiative (FONA) (grant numbers O1LP1920B, O1LP1917D and O1LP2305B). C.K. is funded by the Bundesgesellschaft für Endlagerung through the URS project (research project number STAFuE-21-4-Klei). B.L. is supported by the German palaeoclimate modelling initiative PalMod (grant number O1LP2328A). TI is supported by the European Union’s Horizon 2020 research and innovation programme (ESM2025—Earth System Models for the Future—grant number 101003536), the Deutsche Forschungsgemeinschaft (Germany’s Excellence Strategy—EXC 2037

‘CLICCS—Climate, Climatic Change, and Society’—project number 390683824, contribution to the Center for Earth System Research and Sustainability (CEN) of Universität Hamburg), as well as the European Union’s Horizon 2020 research and innovation programme 4C (grant number 821003). We gratefully acknowledge the European Regional Development Fund (ERDF), the German Federal Ministry of Education and Research and the Land Brandenburg for supporting this project by providing resources on the high performance computer system at the Potsdam Institute for Climate Impact Research.

Author contributions

M.W. and A.G. conceived the study. M.W. designed and performed the model simulations. M.W., C.K., D.D. and B.L. analysed the data and prepared the figures. All authors contributed to the analysis and discussion of the results and the writing of the paper.

Funding

Open access funding provided by Potsdam-Institut für Klimafolgenforschung (PIK) e.V.

Competing interests

The authors declare no competing interests.

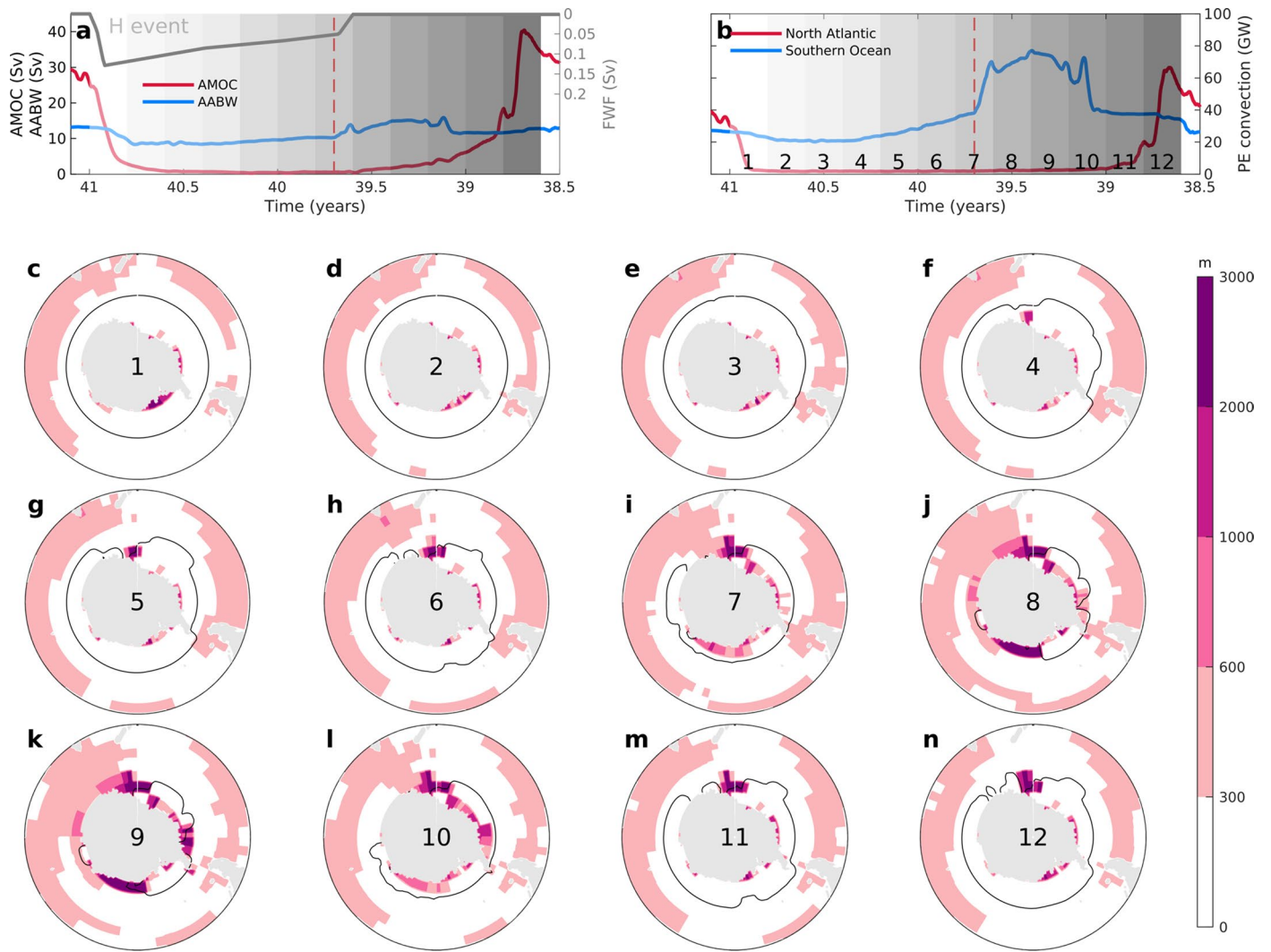
Additional information

Extended data is available for this paper at <https://doi.org/10.1038/s41561-025-01814-0>.

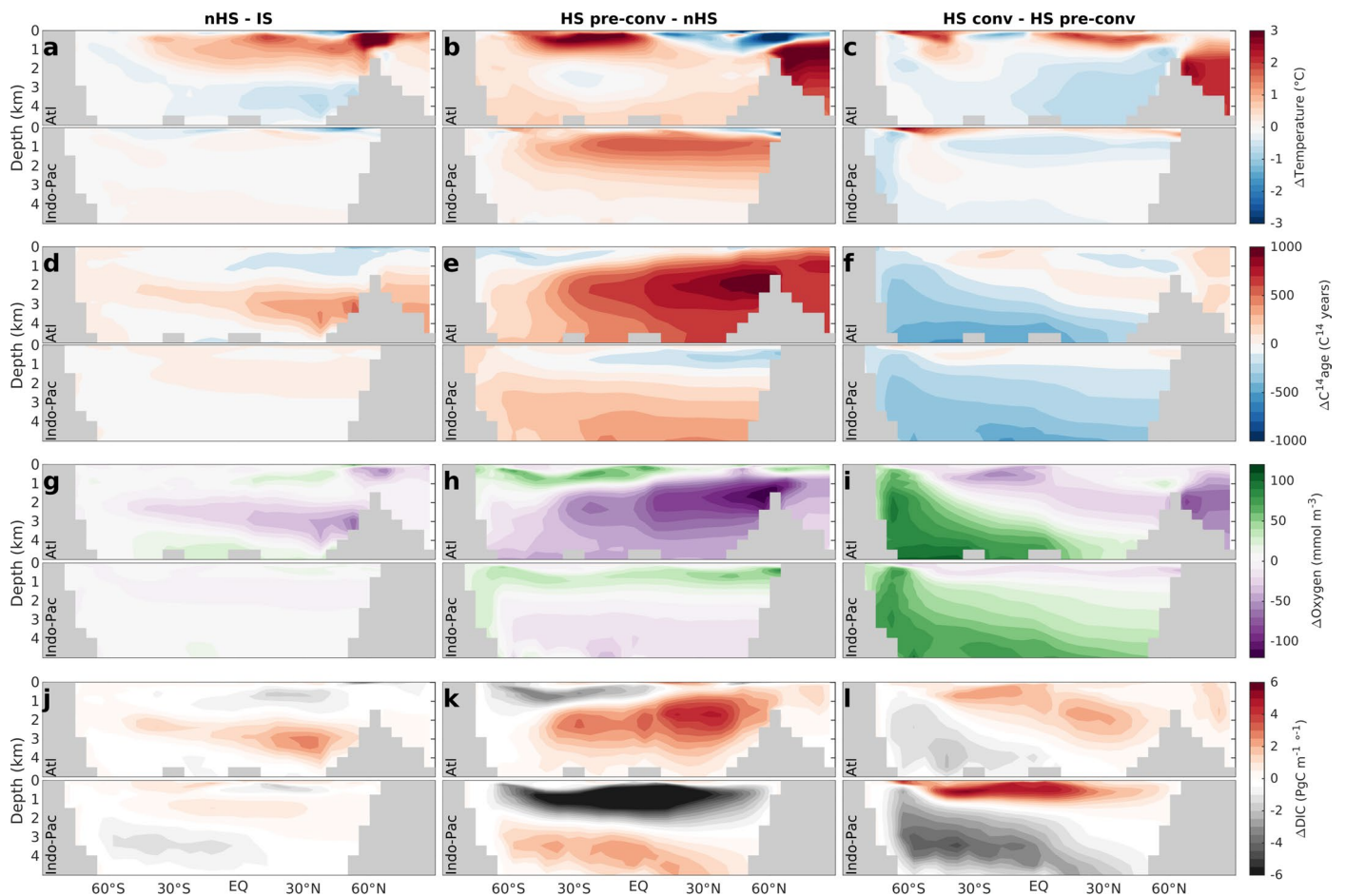
Correspondence and requests for materials should be addressed to Matteo Willeit.

Peer review information *Nature Geoscience* thanks Ran Feng and Aline Govin and the other, anonymous, reviewer(s) for their contribution to the peer review of this work.

Reprints and permissions information is available at www.nature.com/reprints.

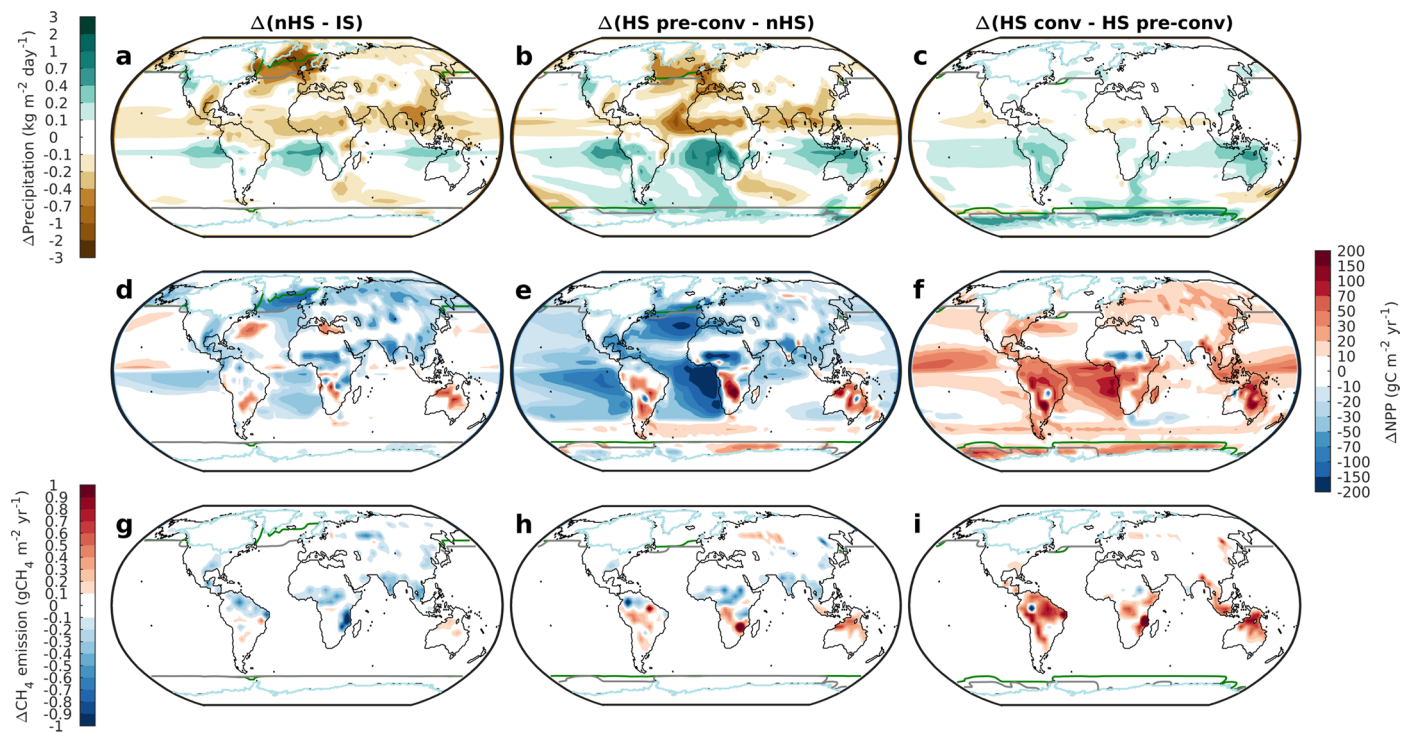


Extended Data Fig. 1 | Evolution of the maximum mixed layer depth in the Southern Ocean during the Heinrich Stadial. c–n Maximum mixed layer depth in the Southern Ocean at different times during the Heinrich Stadial, corresponding to the numbers and shaded grey bars as indicated in **a, b**. Panels **a, b** are the same as those in Fig. 2.



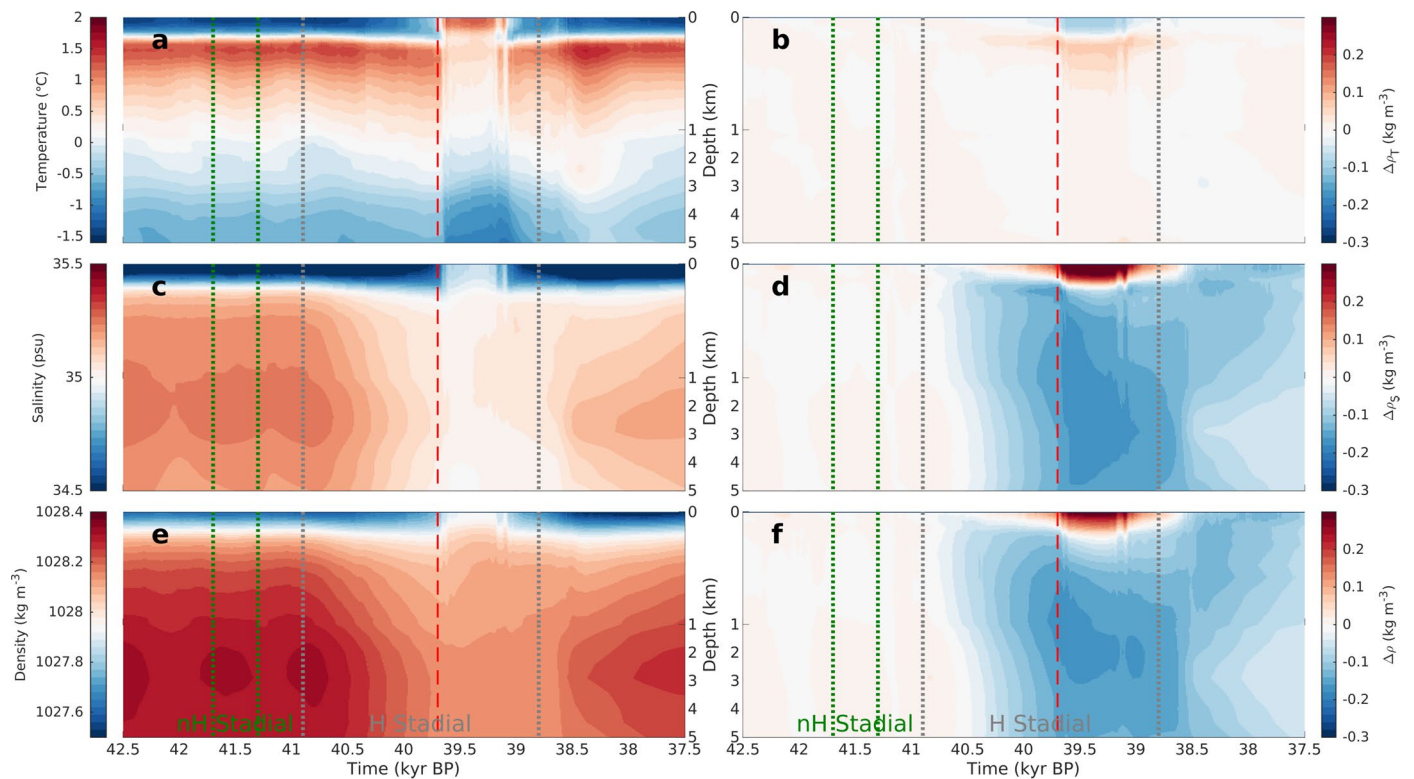
Extended Data Fig. 2 | Ocean response to Dansgaard-Oeschger cycle and Heinrich event. Differences in simulated variables during non-Heinrich Stadial (nHS) relative to Interstadial (IS) (left), Heinrich Stadial (HS) before convection onset relative to non-Heinrich Stadial (middle) and Heinrich Stadial after the onset of convection relative to Heinrich Stadial before convection onset

(right) for **a–c** zonally averaged ocean potential temperature, **d–f** radiocarbon ventilation age, **g–i** oxygen concentration and **j–l** dissolved inorganic carbon. All fields are shown separately for the Atlantic Ocean and the Indo-Pacific Oceans, with the Southern Ocean sectors included.



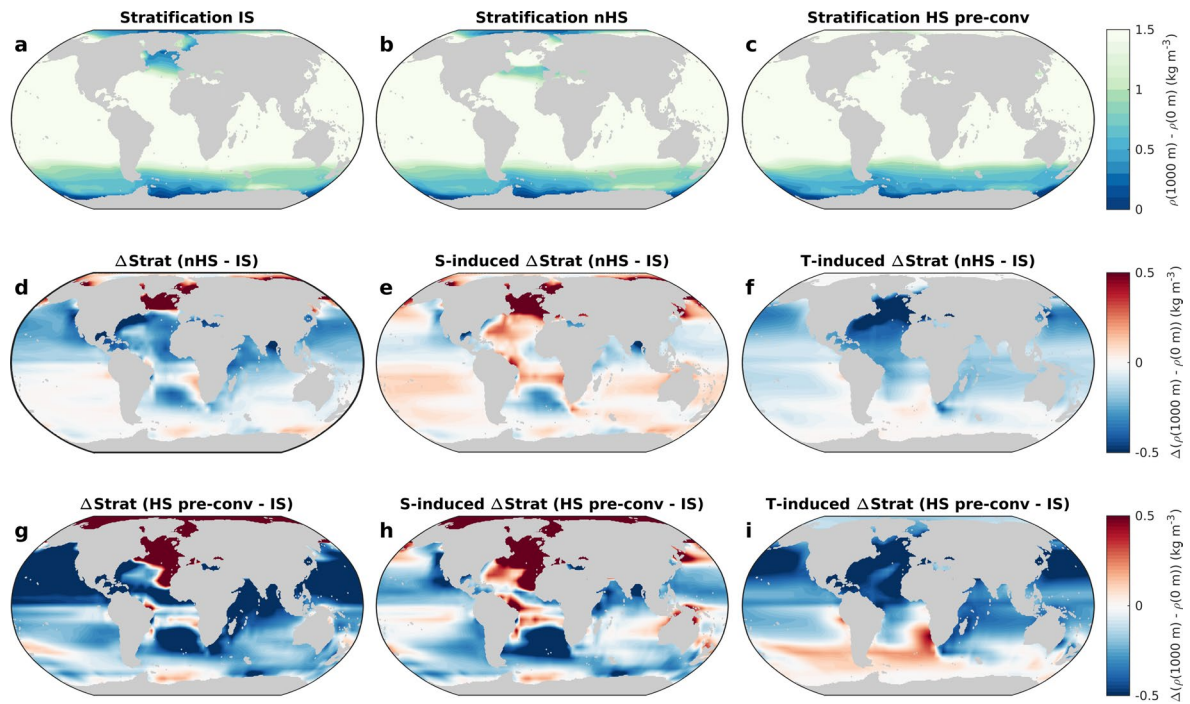
Extended Data Fig. 3 | Changes in precipitation, net primary productivity and CH₄ emissions between different time slices during the Dansgaard-Oeschger/Heinrich cycles. Differences in simulated variables during non-Heinrich Stadial (nHS) relative to Interstadial (IS) (left), Heinrich Stadial (HS) before convection

onset relative to non-Heinrich Stadial (middle) and Heinrich Stadial after the onset of convection relative to Heinrich Stadial before convection onset (right) for **a–c** annual precipitation, **d–f** net primary productivity on land and in the ocean and **g–i** natural CH₄ emissions from wetlands.



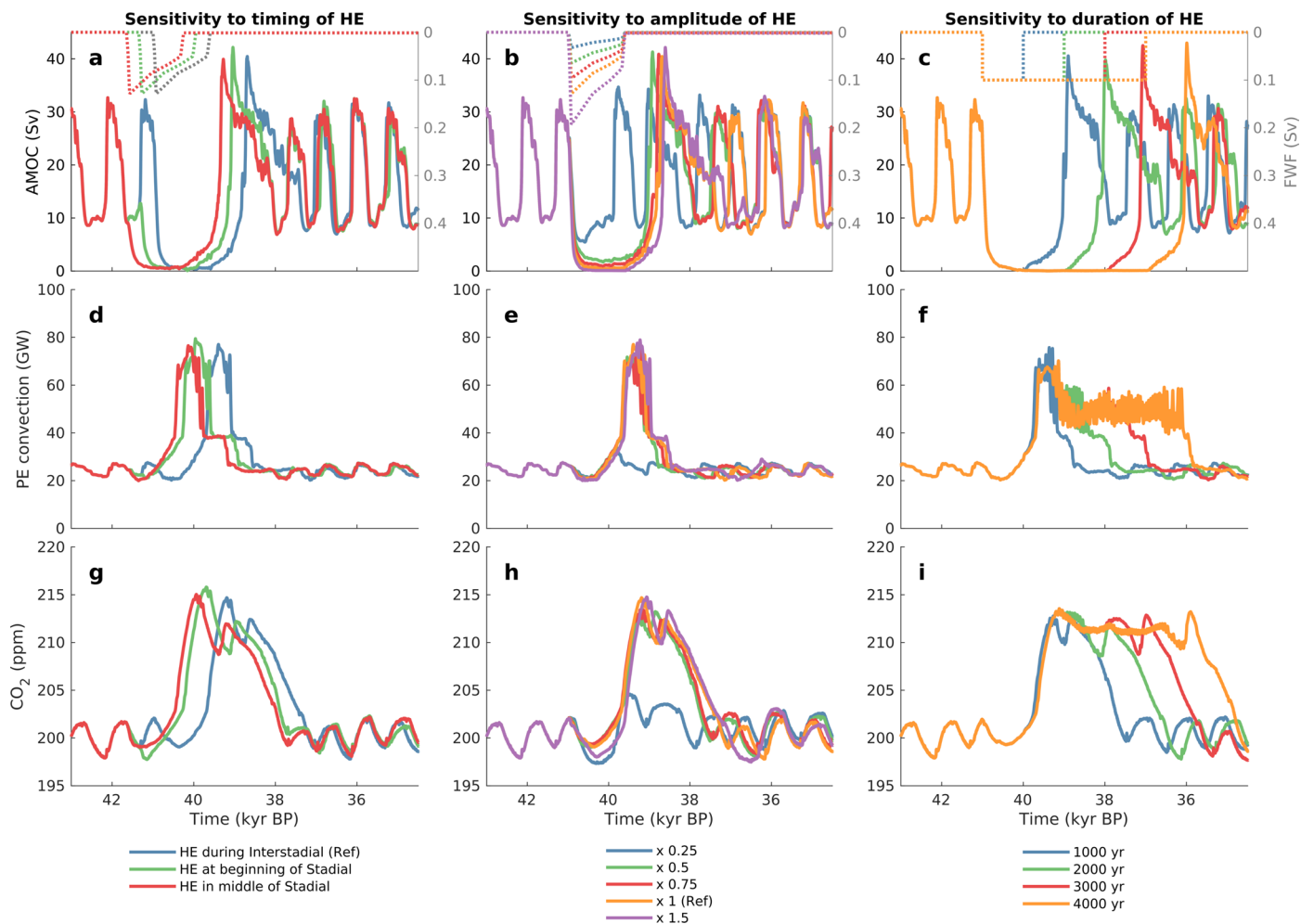
Extended Data Fig. 4 | Ocean temperature, salinity and density evolution in the Southern Ocean. Temporal evolution of vertical profiles of **a** temperature, **c** salinity and **e** density averaged over the Southern Ocean south of 60°S, excluding the Atlantic sector. The right panels show the contributions of **b** temperature and **d** salinity changes relative to average non-Heinrich Stadial

conditions to density changes. The total density changes relative to average non-Heinrich Stadial conditions are shown in **f**. The vertical dotted lines represent the non-Heinrich Stadial (green) and the Heinrich Stadial (grey) and the vertical red dotted line marks the onset of convection in the Southern Ocean.



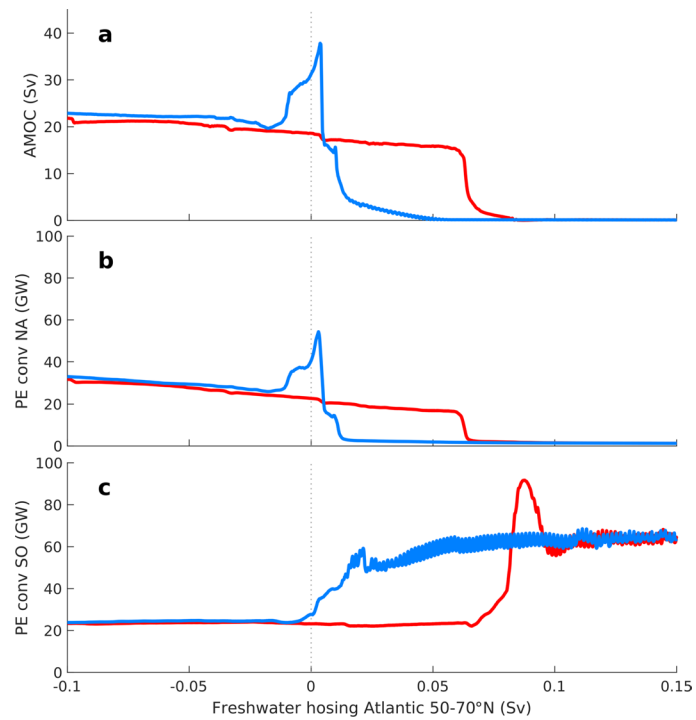
Extended Data Fig. 5 | Ocean stratification. Upper ocean stratification (density difference between 1000 m depth and the surface) for **a** Interstitial (IS), **b** non-Heinrich Stadial (nHS) and **c** Heinrich Stadial (HS) prior to the onset of convection in the Southern Ocean. **d** Change in upper ocean stratification

during the non-Heinrich Stadial relative to the Interstitial with corresponding contributions from **e** salinity changes and **f** temperature changes. **g–i** Same as **d–f** but for the Heinrich Stadial prior to convection onset.



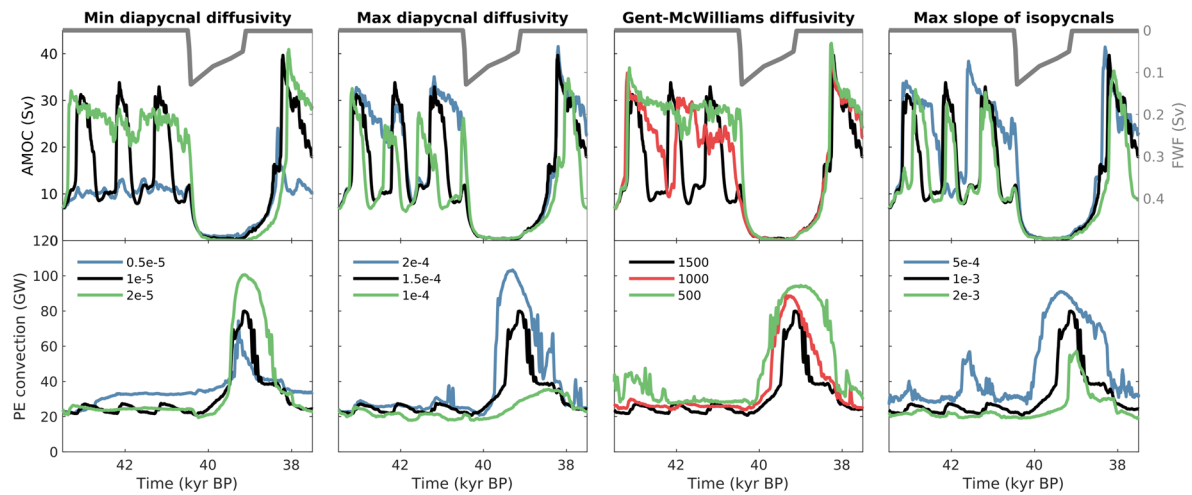
Extended Data Fig. 6 | Sensitivity to timing, amplitude and duration of Heinrich event. Dependence of the simulated AMOC, potential energy released by convection in the Southern Ocean, and atmospheric CO₂ to **a, d, g** the timing, **b, e, h** the amplitude, and **c, f, i** the duration of the Heinrich Event (HE). The

dotted lines in the top panels show the freshwater hosing flux applied to the North Atlantic to mimic the different Heinrich events. The legends at the bottom provide the color code for the different lines.



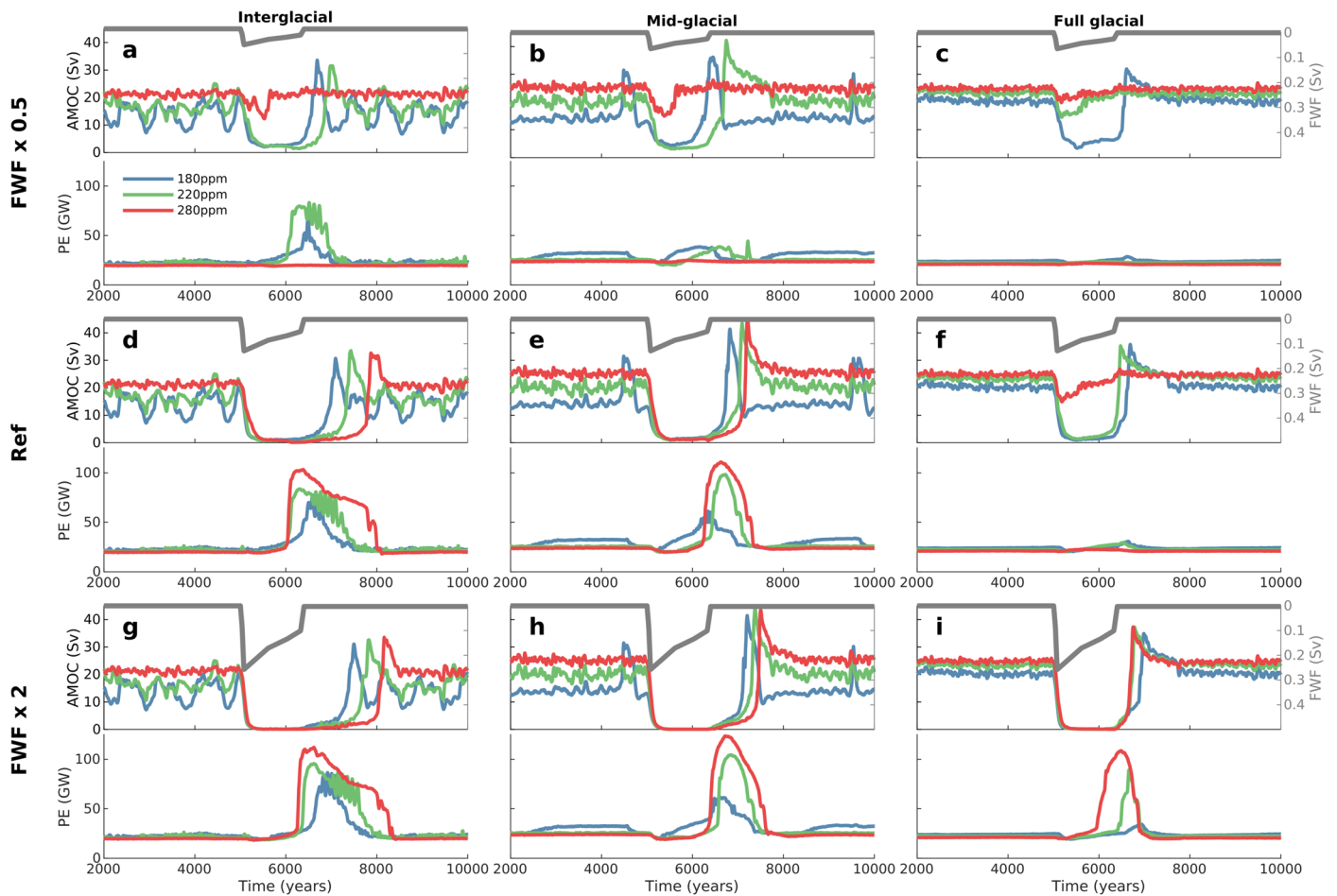
Extended Data Fig. 7 | AMOC hysteresis under mid-glacial conditions. Results from freshwater hysteresis experiments for boundary conditions representative of Heinrich Stadial 4. Freshwater hosing is applied in the latitudinal belt between

50-70°N and increases (red line) or decreases (blue line) at a slow rate of 0.02 Sv/kyr. **a** AMOC strength. Potential energy released by convection in **b** the North Atlantic and **c** the Southern Ocean.



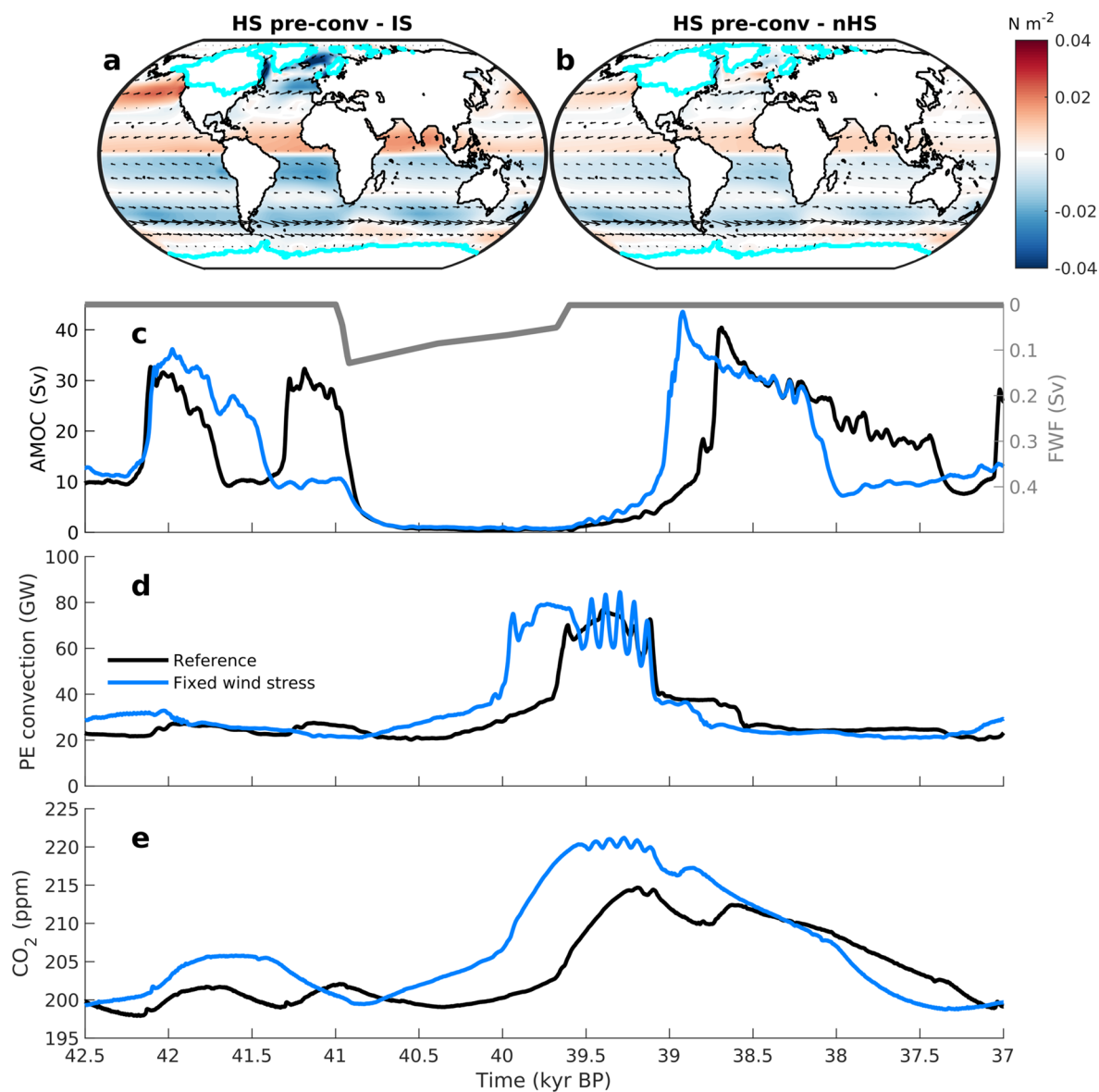
Extended Data Fig. 8 | Sensitivity to ocean model parameters. Dependence of the simulated AMOC and potential energy released by convection in the Southern Ocean to the minimum (surface) value of diapycnal diffusivity ($\text{m}^2 \text{s}^{-1}$), the maximum (deep ocean) value of diapycnal diffusivity ($\text{m}^2 \text{s}^{-1}$),

the Gent-McWilliams diffusivity ($\text{m}^2 \text{s}^{-1}$) and the maximum slope of the isopycnals. The values of the parameters used are given in the legends in the bottom panels. All the experiments are for the same boundary conditions corresponding to the reference model simulation presented in the paper.



Extended Data Fig. 9 | Sensitivity to ice sheets and baseline atmospheric CO₂ for different amplitudes of the Heinrich event. Maximum of the AMOC streamfunction and potential energy released by convection in the Southern Ocean for model simulations with **a, d, g** interglacial (present-day) ice sheets

(left), **b, e, h** mid-glacial ice sheets (middle) and **c, f, i** full glacial (LGM) ice sheets (right) with different amplitudes of the Heinrich event (increasing from top to bottom) and different prescribed constant CO₂ concentrations (180, 220 and 280 ppm) as indicated by the colored lines and the legend.



Extended Data Fig. 10 | Sensitivity to wind stress. Changes in simulated wind stress over the ocean between Heinrich Stadial prior to the onset of convection in the Southern Ocean and **a** Dansgaard-Oeschger Interstadial and **b** non-Heinrich Stadial. Comparison of simulated evolution of **c** maximum of the

Atlantic meridional overturning streamfunction, **d** potential energy released by convection in the Southern Ocean and **e** atmospheric CO₂ in the reference run (black) and in a simulation where the (seasonally varying) wind stress over the ocean is prescribed to average non-Heinrich Stadial conditions (blue).